Journal of Catalysis **182,** 186–198 (1999)
Article ID jcat.1998.2348, available online at http://www.idealibrary.com on IDEAL®

# EXAFS Studies of Supported Rh–Sn Catalysts for Citral Hydrogenation

Laura Sordelli,* Rinaldo Psaro,* Gilberto Vlaic,† Anna Cepparo,† Sandro Recchia,* Carlo Dossi,* Achille Fusi,* and Robertino Zanoni‡

*CNR Research Centre "CSSCMTBSO" and Dipartimento di Chimica Inorganica, Metallorganica e Analitica, Università degli Studi di Milano, Via Venezian 21, 20133 Milan, Italy; †Dipartimento di Scienze Chimiche, Universita' di Trieste, Via L.Giorgieri 1, & Elettra S.p.A, Trieste, Italy; and ‡Dipartimento di Chimica, Universita' La Sapienza di Roma, Piazzale A. Moro 5, 00185 Rome, Italy

Received July 8, 1998; revised October 12, 1998; accepted November 8, 1998

**Rh–Sn/$SiO_2$ bimetallic catalysts were prepared by "traditional" coimpregnation with aqueous solutions of $RhCl_3$ and $SnCl_2$. Their catalytic properties were used to study the mechanism of tin promotion in the liquid-phase selective hydrogenation of citral. The structural evolution during the activation treatments has been investigated by in situ EXAFS spectroscopy. As a function of the activation treatment used, different bimetallic phases have been detected, depending on the extent of the coordination of tin to rhodium atoms. The parallel use of $H_2$ chemisorption measurements gave complementary information on the surface composition of the bimetallic particles. A freshly calcined–reduced sample may be described as a cherry-like structure, which is selective for the formation of unsaturated alcohols. On the contrary, an alloy-type phase obtained by simple reduction is totally unselective.**

**The production of unsaturated alcohols starts only after an induction period during which the catalyst surface restructures, and tin oxides moieties on rhodium particle surface are produced. The selective activation of the carbonyl bond is attributed to the interaction with the tin oxide moieties present in the bimetallic phase.** 

## INTRODUCTION

The reaction of unsaturated aldehydes may be described as a parallel consecutive network (1) in which one or both of the unsaturated functionalities may be hydrogenated. Three metals with the greatest potential are Pt, Ru, and Rh. On inert supports, all three metals tend to be more selective to the saturated aldehyde (SAL) than to the unsaturated alcohol (UOL). However, in the hydrogenation of cinnamaldehyde, the selectivity to UOL can be enhanced with changes in the nature of the support (2), in the presence of promoters (3), or with changes in the metal particle size and morphology (4, 5). The structure sensitivity of the crotonaldehyde hydrogenation over supported Pt catalysts has been recently reported by English *et al.* (6), showing that the selectivity to UOLs increases with increasing particle size.

In general, looking for the effects of chemical promotion, it is known that the addition of a suitable promoter (Sn, Ge, Fe, Ga) gives an improvement in the UOL selectivity (7). In addition to a geometric effect of the second metal, which decreases the number of contiguous platinum atoms, thus dividing the platinum surface into smaller ensembles (8), two models based on electronic effects have been proposed to explain the improvement in selectivity. The first one is based on the observation that an increased electron density on the base metal can be induced by the formation of metal alloys or by a strong interaction with the promoter (or with the support). The probability for C=C double bond adsorption is thus decreased and, at the same time, the interaction of a C=O bond is promoted. The second model is based on the presence of surface Lewis acid sites ($Sn^{n+}$ or $Ge^{n+}$) at or near the metal particles that may interact with the lone electron pairs of the carbonyl group oxygen. The effect of electrophiles on a carbonyl group is a well-known process in coordination chemistry (9), which implies a dramatic increase in the rate of CO insertion in metal–alkyl bonds. In the selective hydrogenation of $\alpha,\beta$-unsaturated aldehydes, the acidic sites would favour the coordination of the multifunctional molecule through its aldehydic fragment and, following the lowering of the C=O bond strength, a higher rate of hydrogenation can be obtained.

Also, the structure of the substrate plays a critical role. Steric hindrance around the C=C bond facilitates the selective hydrogenation of the carbonyl group, whereas a lack of substituents on the C=C bond make this selective hydrogenation more difficult (10). In contrast to what is observed for cinnamaldehyde, in the citral hydrogenation no dependence on the ruthenium particle size has been observed, either on the reaction rate or on the selectivity (5). The difference has been ascribed to the presence/absence of the aromatic ring in the molecule and to its steric effect.

In the case of citral, a variety of extremely active and selective $Rh[Sn(n\text{-}C_4H_9)_x]_y/SiO_2$ bimetallic catalysts have been obtained by partial hydrogenolysis of $Sn(C_4H_9)_4$ on the surface of $Rh/SiO_2$ (11). By XPS measurements, it was found that the majority of tin is in an oxidised state (II or IV), suggesting that the Lewis acid properties of the Sn atoms activate the carbonyl group. A geometric effect, due



0021-9517/99 $30.00

to the presence of Sn surrounded by organic alkyl chains, cannot be ruled out.

The positive effect of tin on the selective hydrogenation of citral has been reported also for $Ru/Al_2O_3$ catalysts obtained by the controlled surface reaction method (12). The EXAFS and Mössbauer experiments carried out after in situ reduction have shown neither the formation of Ru–Sn bonds nor the presence of metallic tin. It can therefore be suggested that the positive effect of tin is mainly related to the formation of Sn ions.

The $Rh–Sn/SiO_2$ systems, prepared by impregnation of both metals or by Rh impregnation and Sn deposition by CVD (13, 14), have been characterised by TEM, $H_2$/CO chemisorption, IR, and EXAFS spectroscopies (13, 14) at different Sn contents. The EXAFS data showed a dominant contribution of metallic tin after reduction, forming both Sn–Rh and Sn–Sn bonds. Moreover, depending on the preparation method (14), the tin atoms are preferentially located at the surface or in the bulk of the bimetallic particles.

The methodology used for the catalyst preparation has thus been shown to be crucial in the determination of the catalytic properties which, in turn, are related to the structural properties. The characterisation of supported bimetallic systems requires the investigation of several factors, such as the bulk and surface relative composition, the presence of several possible different alloy phases, and the coexistence of one or both metals in different oxidation states.

With the aim of clarifying the relationship between structure and catalytic properties of tin-promoted silica-supported Rh catalysts, we decided to study a catalyst produced with the traditional coimpregnation technique from the corresponding chloride salts. The influence of different catalyst activation treatments on the citral selective hydrogenation was also examined.

The influence of electronic effects induced by the interaction with the support was also studied and magnesia was used as a basic support. The structural characterisation of Rh–Sn catalysts supported on silica and on magnesia has been performed by EXAFS spectroscopy. EXAFS is, in fact, sensitive to short-range ordering and can provide unique structural information for highly dispersed catalysts (15), especially for bimetallic systems where the analysis is feasible at both metal edges (16). Moreover, the possibility of recording the spectra in situ allows us to investigate the structural evolution during the activation treatments (17) and to check the determining step in the growing of the catalitically active bimetallic particles.

## EXPERIMENTAL

### *Catalyst Preparation*

The starting supports were $SiO_2$ (Davison 62A, 200 $m^2/g$) and MgO (Carlo Erba, 200 $m^2/g$). The monometallic Rh catalysts were prepared by impregnation of the support with an aqueous solution of $RhCl_3$. Bimetallic samples were prepared by the traditional coimpregnation technique using aqueous solutions of $RhCl_3$ and $SnCl_2$. All samples, after drying, were calcined under $O_2$ (50 ml/min) and reduced under flowing $H_2$ (50 ml/min) at 773 K for 1 h after a heating ramp of 10 K/min. The catalysts were then brought into the reactor under $N_2$.

The catalytic tests and the EXAFS characterization were carried out on samples with a rhodium loading, determined by atomic absorption spectroscopy (AAS), of $4.0 \pm 0.1$ wt%, with a Sn/Rh molar ratio of 0.5. All samples used for the $H_2$ chemisorption had a rhodium loading of $2.0 \pm 0.1$ wt% (Sn/Rh = 0.5).

### *Catalytic Studies*

The hydrogenation of citral (Aldrich C8, 300-7, purity 95%) has been carried out in a 100-ml glass batch reactor thermostatted at 308 K, under $H_2$ atmosphere. Typically 20 ml of a 1 : 200 (v/v) citral : *n*-heptane solution was loaded into the reactor; the amount of catalyst was weighted in order to have a substrate/rhodium molar ratio of about 200.

A series of catalytic tests, performed by varying the tin content, allowed us to establish the better Sn/Rh ratio for the selectivity to unsaturated alcohols. This kind of optimisation was carried out on the silica-supported catalysts only, and a typical volcano curve was obtained by plotting the selectivity vs the Sn/Rh ratio. The maximum corresponds to a Sn/Rh value between 0.5 and 0.6. A rapid deactivation is observed for Sn/Rh > 1. The Sn/Rh value of 0.5 was then fixed for all systems, and the metal loading was kept constant for each test.

The reaction was followed through the analysis of a sufficient number of microsamples. Quantitative analysis was performed with GC-MS instrumentation (Helwett–Packard MSD 5971) equipped with a DB-225 J&W column (0.23 mm i.d. × 30 m length). Catalytic conversions are calculated on citral consumption. Yields to nerol + geraniol (unsaturated alcohols, UOLs) are reported as

$$(\text{moles of UOLs})/(\text{total moles of reacted citral}) \times 100.$$

Yields to citronellal (saturated aldehydes, SALs) and to acetal are reported similarly.

Preliminary tests, with different amounts of catalyst and stirring rate, were carried out in order to ascertain the absence of diffusion limitations.

### *Hydrogen Chemisorption*

The amounts of $H_2$ adsorbed on the catalysts were measured in the pulse flow mode using a Micromeritics Pulse Chemisorption 2700 apparatus. Chemisorption measurements were carried out at 348 K with $H_2$ pulses of 50 $\mu$l, after a standard oxidation–reduction cycle at 673 K.

The chemisorption temperature was decided after a temperature hydrogen desorption measurement from 223 to 773 K and is in good agreement with chemisorption temperatures reported for rhodium-supported materials (18). More detailed information about apparatus and procedures is reported elsewhere (19).

*EXAFS*

X-ray absorption spectra were collected at the GILDA beamline of the ESRF (Grenoble, France) operating at 6 GeV of electron energy and a storage ring current of 70–90 mA (in the 16-bunch mode). The experimental station is equipped with a Si(311) double crystal saggittal dynamical focusing monochromator (20), which provides a beam size at the sample of $1 \times 1$ mm$^2$ in the 5–30 keV spectral range. The energy resolution is $\Delta E/E = 10^{-5}$–$10^{-4}$ and the photon flux at the sample is $10^{10}$–$10^{11}$ ph s$^{-1}$ (0.01% bw, 0.1A). Third harmonic rejection is achieved by detuning the two Si crystals; second harmonics are absent due to the extinction rule of the Si(311) crystal. Spectra were recorded on the same sample at the Rh and Sn edges consecutively, with a double angle/energy calibration for each sample, using both Rh and Sn metal foils.

All spectra were recorded at 300 K in transmission mode at the Rh and Sn *K*-edge over the range 23–24.2 and 29–30.2 keV, respectively, with a sampling step of 2 eV and an integration time of 2 s for each point. Incident and transmitted photon fluxes have been detected with ionisation chambers filled, respectively, with 0.1 and 0.4 bar of Kr. Each spectrum has been acquired three times. The powder samples were loaded under inert atmosphere, reduced in situ in $H_2$ flow at 623 K in a catalysis–EXAFS cell (Lytle type), and cooled to room temperature before spectra acquisition. Sample homogeneity was checked by reading the transmitted photocurrent while scanning the sample area along the *x*-*y* axes.

Extracted $\chi(k)$ data have been averaged before the EXAFS data analysis. The standard deviation calculated from the averaged spectra was used as an estimate of the statistical noise for the evaluation of the errors associated with each structural parameter (21). Experimental $\chi(k)$ data were extracted from absorption data by a conventional procedure outlined as follows: a linear background was fitted in the pre-edge region, extrapolated to higher energies, and then subtracted from absorption data. The atomic-like contribution was estimated by a 5th degree polynomial fit and then subtracted from experimental data following the procedure proposed by Lengeler and Eisenberger (22). The result was normalised to edge height to obtain the experimental $\chi(k)$. The $k^3$-weighted $\chi(k)$ data were Fourier transformed over a Kaiser window, with $\tau = 2.5$, in a typical $k$ range of 3–14 Å$^{-1}$. Main contributions to the Fourier transform modulus were filtered in order to obtain metal nearest-neighbour shells. The filtered contributions thus obtained were analysed using the programs developed by Michalowicz (23), whose nonlinear least-squares fit exploits the minimisation capabilities of the MINUIT program (24). Phase shift and amplitude functions of scattering atoms have been extracted from the experimental spectra of the following model compounds: Rh foil, Sn foil, $Rh_2O_3$, $SnO_2$, $RhCl_3/SiO_2$ 10%, and $SnCl_2/SiO_2$ 10%. It is not possible to distinguish the Rh and Sn scatterers from each other, since the scattering amplitude and phase functions are very similar. In the following we always refer to the averaged values Rh–*M* and Sn–*M* (*M* = Rh, Sn).

Whenever necessary the statistical significance of the results obtained was checked by applying the *F*-test proposed by Joyner *et al.* (25).

## RESULTS

*EXAFS Data*

The EXAFS analysis has been performed on the monometallic $RhCl_3/SiO_2$ and on the bimetallic $RhCl_3$–$SnCl_2/SiO_2$ and $RhCl_3$–$SnCl_2$/MgO (molar ratio Sn/Rh = 0.5) catalysts after each activation treatment applied to the freshly impregnated samples (i.e., ex situ calcination and in situ reduction).

Spectra have been recorded at both metal *K*-edges but, due to the noise level at the Sn edge (because of the lower concentration and higher transparency of tin, and of the Rh simultaneous absorption), all fits here reported have been performed for the Rh edge spectra only. Qualitative information, however, has been extracted also from the Sn edge data.

The supported $RhCl_3/SiO_2$ and $SnCl_2/SiO_2$, at the 10 wt% loading level, have been used as reference compounds for the experimental phase and amplitude function extraction of both the metal chlorides. The correctness of this procedure has been proved by fitting the supported references with the structural parameters of the pure salts and the theoretical FEFF7 phase and amplitude functions, obtaining a perfect agreement.

The crystallographic parameters of the reference compounds used to extract experimental phase and amplitude functions are reported in Table 1; the results of the fits are summarised in Table 2.

*Rh/SiO$_2$.* The FT spectrum of the $RhCl_3/SiO_2$ (4 wt%) sample just impregnated corresponds to that of the reference used for Rh chloride ($RhCl_3/SiO_2$, 10 wt%), exhibiting only a large peak at about 2 Å (not phase corrected) corresponding to the Cl shell. The fit calculated over the filtered range $\Delta R = 1$–3 Å gives 5.7 Cl atoms at 2.30 Å.

After the calcination treatment, the inspection of the modulus of the FT spectrum in Fig. 1 reveals that a three-shell structure is present. A fitting procedure of the filtered region $\Delta R = 0.84$–3.27 Å, comprising all three shells, revealed the contribution of Rh–O, Rh–Cl, and Rh–Rh shells.

**TABLE 1**

**Crystallographic Parameters of Reference Compounds Used for Experimental Phase and Amplitude Extraction**

| Sample | Shell | $N$ | $R$ (Å) | $\sigma$ (Å)[a] |
|---|---|---|---|---|
| Rh foil | Rh | 12 | 2.687 | 0.07 |
| Sn foil | Sn | 4 | 3.022 | 0.07 |
| | Sn | 2 | 3.176 | 0.07 |
| $RhCl_3/SiO_2$ 10% imp | Cl | 6 | 2.310 | 0.07 |
| $Rh_2O_3$ | O | 6 | 2.048 | 0.07 |
| $RhO_2$ | O | 6 | 1.963 | 0.07 |
| $SnO_2$ | O | 6 | 2.068 | 0.07 |

[a] Arbitrary values used in experimental amplitude function extraction.

Due to the correlation between the $N_i$, and $\sigma_i$ parameters produced by the shell overlapping, the fit converges within a value interval of the previous parameters, with the same statistical probability. Despite the large error bars reported in Table 2, to account for the uncertainty among the different fits, it is evident that the oxidation produces a mixed-phase structure, where part of the Rh is still present as chloride and part as oxide or, possibly, oxychloride species.

After the reduction at 400°C, the FT spectrum exhibits all the features of the Rh foil up to the fourth shell (Fig. 2), and the first shell fit gives 10.5 Rh atoms at 2.69 Å, which means large Rh clusters with fcc structure. Cl is no longer detected.

A further in situ calcination at 400°C (not reported in Table 2) on a previously calcined–reduced sample produces a completely oxidised Rh, where the first shell fit gives values coincident with those of $Rh_2O_3$.

*Rh–Sn/$SiO_2$.* The comparison between the FT spectra of the Rh–Sn/$SiO_2$ sample freshly impregnated and the $RhCl_3/SiO_2$ reference shows that, apart from a slight height reduction, the presence of $SnCl_2$ does not affect the chemical surrounding of Rh atoms. The best fit for the inverse Fourier transform of the first peak filtered region, $\Delta R = 1.21$–$2.39$ Å, reveals the presence of a single shell of six Cl atoms around the Rh absorber at almost the same distance as in the $RhCl_3$ crystal (2.303 Å vs 2.310 Å). The introduction of an additional oxygen or metal shell, to include the possible presence of the support or of the promoter metal, gives a fit which is statistically not more significant, as evaluated by the *F*-test. The Sn–O phase-corrected FT spectrum at the Sn edge shows a single oxygen peak at about 2.13 Å, indicating that just after impregnation the tin is completely surrounded by oxygen atoms.

The FT spectrum at the Rh edge of the same sample after oxidation, shown in Fig. 3, exhibits two distinct peaks at distances of about 1.5 and 2 Å (not phase corrected), which can correspond to Rh–O in the Rh oxide and Rh–Cl in the Rh chloride. The fit obtained on the basis of a two-shell model reaches the best quality factor for 2 O at 2.005 Å (to be compared with the 2.048 Å in $Rh_2O_3$) and 3 Cl at 2.330 Å (versus the 2.310 Å of the $RhCl_3$), for a total of five neighbours around the Rh. The low intensity of the FT spectrum is due to the phase opposition between O and Cl as scatterers, which produces destructive interference.

In Fig. 4 (note the different scale) is shown the comparison of the FT imaginary part and modulus between the metal foil and the calcined Rh–Sn/$SiO_2$ after in situ reduction. The two spectra have a strong resemblance in the first peak, but there is no correspondence between the outer

**TABLE 2**

**Curve Fitting Results of the Rh *K*-Edge EXAFS Data**

| Sample[a] | Treatment | Shell | CN | $R$ (Å) | $\Delta\sigma$ (Å) | $\Delta E_0$ (eV) |
|---|---|---|---|---|---|---|
| $Rh/SiO_2$ | — | Cl | $5.7 \pm 0.2$ | $2.300 \pm 0.002$ | $0.069 \pm 0.003$ | $-1.0 \pm 0.2$ |
| $Rh/SiO_2$ | $O_2$ | O | $4 \pm 1$ | $2.00 \pm 0.01$ | $0.09 \pm 0.04$ | $2 \pm 2$ |
| | | Cl | $2 \pm 1$ | $2.33 \pm 0.03$ | $0.05 \pm 0.02$ | $0 \pm 10$ |
| | | Rh | $2 \pm 1$ | $3.05 \pm 0.02$ | $0.11 \pm 0.01$ | $8 \pm 2$ |
| $Rh/SiO_2$ | $O_2$–$H_2$ | Rh | $10.5 \pm 0.3$ | $2.692 \pm 0.002$ | $0.076 \pm 0.001$ | $0.4 \pm 0.1$ |
| $RhSn/SiO_2$ | — | Cl | $5.9 \pm 0.1$ | $2.303 \pm 0.002$ | $0.066 \pm 0.002$ | $1.41 \pm 0.20$ |
| $RhSn/SiO_2$ | $O_2$ | O | $1.9 \pm 0.1$ | $2.005 \pm 0.005$ | $0.072 \pm 0.004$ | $-3.42 \pm 1.00$ |
| | | Cl | $3.0 \pm 0.1$ | $2.330 \pm 0.004$ | $0.082 \pm 0.003$ | $4.70 \pm 0.70$ |
| $RhSn/SiO_2$ | $O_2$–$H_2$ | M | $6.8 \pm 0.3$ | $2.722 \pm 0.002$ | $0.106 \pm 0.002$ | $-4.76 \pm 0.25$ |
| $RhSn/SiO_2$[b] | $H_2$ | M | $7.6 \pm 0.1$ | $2.752 \pm 0.001$ | $0.109 \pm 0.001$ | $-3.71 \pm 0.13$ |
| RhSn/MgO | — | O | $5.0 \pm 0.9$ | $2.055 \pm 0.015$ | $0.072 \pm 0.013$ | $2.70 \pm 0.80$ |
| | | Cl | $1.2 \pm 0.5$ | $2.31 \pm 0.03$ | $0.072 \pm 0.013$ | $1.80 \pm 0.50$ |
| RhSn/MgO | $O_2$ | O | $7.4 \pm 0.1$ | $2.081 \pm 0.001$ | $0.083 \pm 0.001$ | $4.41 \pm 0.09$ |
| RhSn/MgO | $O_2$–$H_2$ | O | $1.0 \pm 0.5$ | $2.076 \pm 0.005$ | $0.094 \pm 0.004$ | $3.70 \pm 0.10$ |
| | | M | $7.7 \pm 0.3$ | $2.746 \pm 0.003$ | $0.114 \pm 0.004$ | $3.50 \pm 0.5$ |

[a] Rh loading = 4 wt%; Sn/Rh molar ratio = 0.5.

[b] Fresh catalyst has been pretreated in $H_2$ flow at 773 K. All the other samples have been exposed to a calcination–reduction cycle at 773 K.

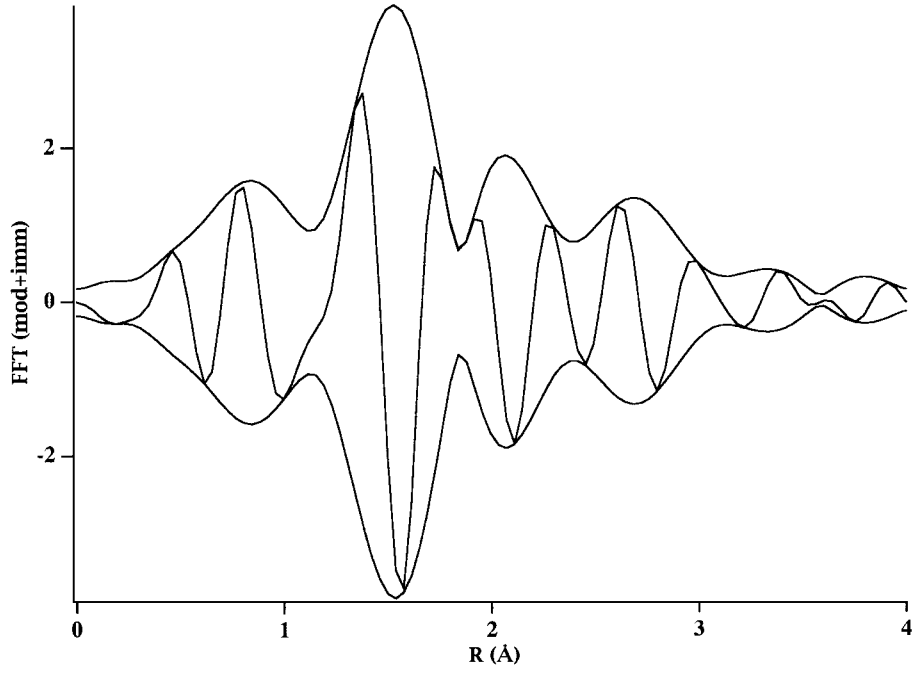


**FIG. 1.** Fourier transform modulus and imaginary part (not phase corrected) of the Rh *K*-edge $k^3$-weighted EXAFS data of $Rh/SiO_2$ after calcination. $\Delta k = 3$–$14$ Å$^{-1}$.

shells. The fit of the first shell performed with experimental phase and amplitude functions extracted from the Rh foil gives 6.8 metal nearest neighbours at 2.722 Å. We also tried to model the simultaneous presence of both Rh and Sn but without any valuable results due to the above-mentioned similarity of the amplitude function for the two metals. We therefore agree with Iwasawa and Yoshikawa (14) and assume that it is not possible to distinguish between the Rh

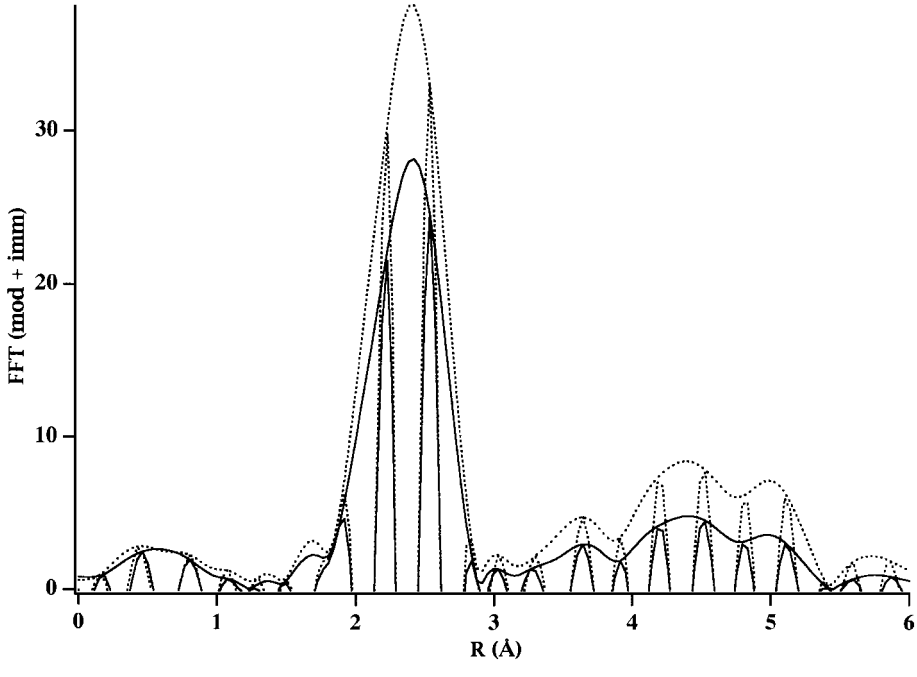


**FIG. 2.** Fourier transform moduli and imaginary parts (not phase corrected) of the Rh *K*-edge $k^3$-weighted EXAFS data of $Rh/SiO_2$ after calcination and reduction (solid line) and of Rh foil (dotted line). $\Delta k = 3$–$14$ Å$^{-1}$.

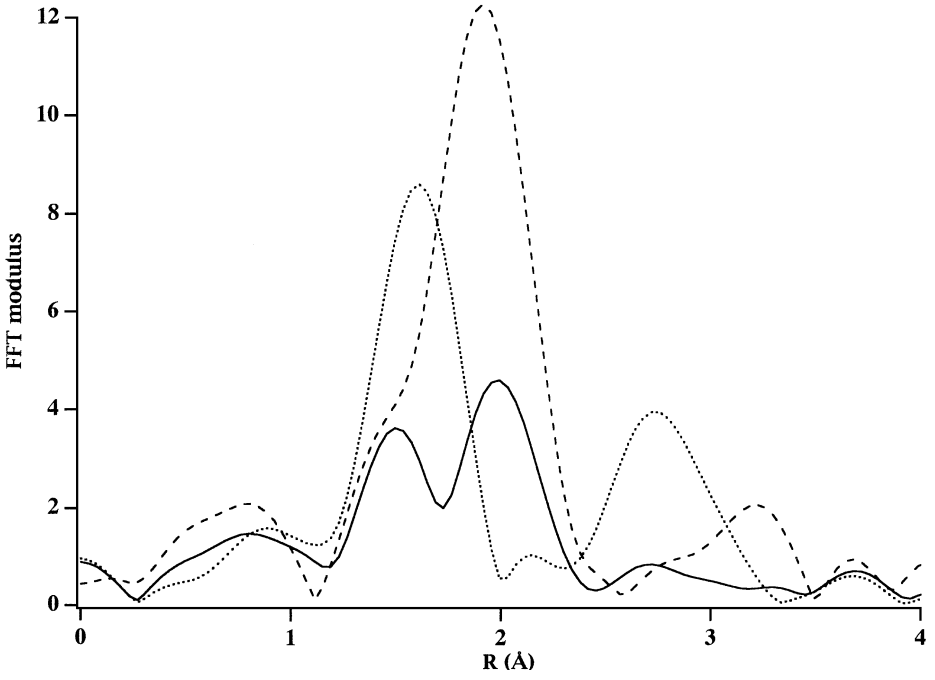


**FIG. 3.** Fourier transform moduli (not phase corrected) of the Rh *K*-edge $k^3$-weighted EXAFS data of Rh–Sn/$SiO_2$ after calcination (solid line), of Rh foil (dashed line) and of $Rh_2O_3$ (dotted line). $\Delta k = 3.9$–$14$ Å$^{-1}$.

and Sn contribution. The long Rh–metal distance found in the single-shell fit could be an average value between the two-metal contribution, and the high $\sigma$ value an indication of the high structural disorder due to a mixed phase.

The comparison between the FT spectra of the Rh–Sn/$SiO_2$ samples after a simple reduction treatment and after the usual calcination–reduction cycle indicates that the only relevant difference is a slight shift in the main peak

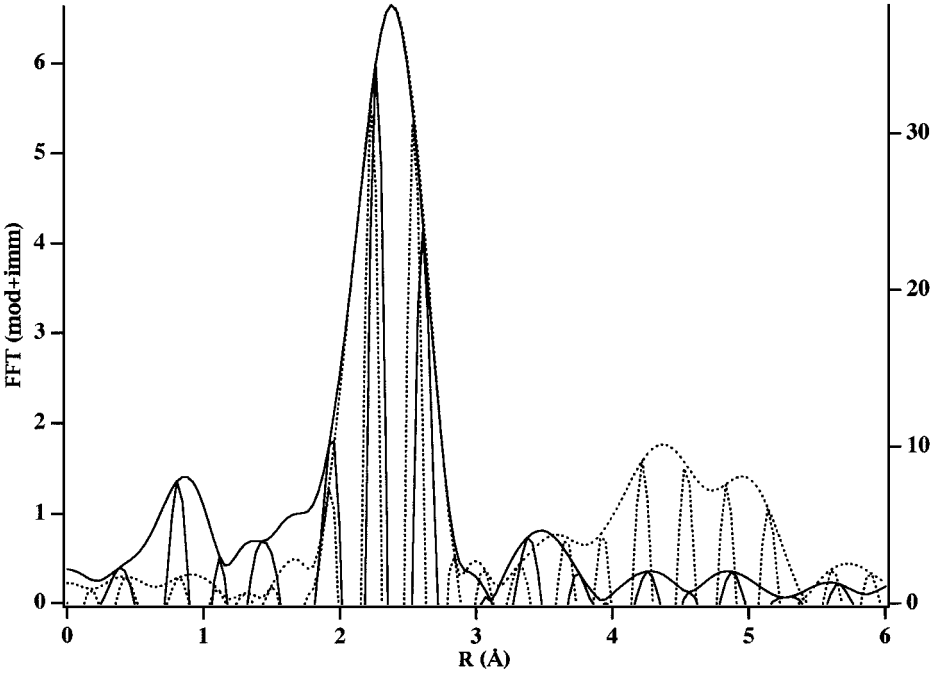


**FIG. 4.** Fourier transform moduli and imaginary parts (not phase corrected) of the Rh *K*-edge $k^3$-weighted EXAFS data of Rh–Sn/$SiO_2$ after calcination and reduction (solid line; left axis) and of Rh foil (dotted line; right axis). $\Delta k = 3.9$–$14$ Å$^{-1}$.

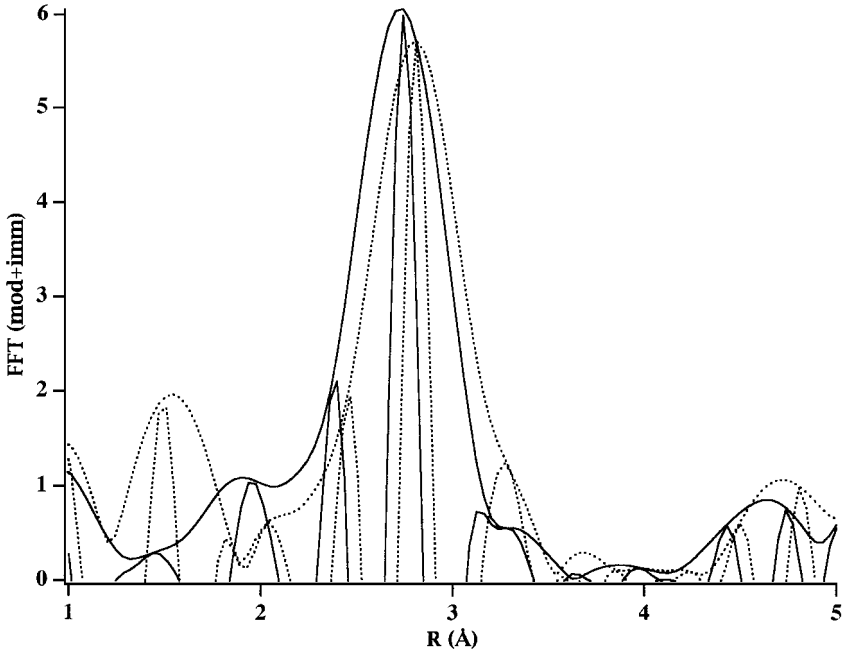


**FIG. 5.** Comparison of the Sn–Sn phase-corrected Fourier transform moduli and imaginary parts of the Sn *K*-edge $k^3$-weighted EXAFS data of Rh–Sn/$SiO_2$ after impregnation–reduction (solid line) and after impregnation–calcination–reduction (dotted line). $\Delta k = 3$–$12$ Å$^{-1}$.

maxima, the simply reduced one occurring at longer distance (2.752 Å vs 2.722 Å). We also tried to introduce the shoulder present in the lower part of both spectra as a Cl contribution, but it added no improvement in the fit.

The presence of some residual Cl should be expected, as in a similar monometallic Rh/$SiO_2$ $RhCl_3$-derived sample previously studied by Gloor and Prins (26), a small amount of Cl atoms were detected after calcination–reduction treatment under similar conditions. It should be noticed that in our case the metal clusters are relevantly larger (first shell CN = 6.8 versus 3.6) so that the Cl contribution should be masked by the amplitude of the metal signal.

In Fig. 5 is shown the comparison between the imaginary parts and moduli of the FT spectra (Sn–Sn phase corrected) at the Sn edge of the Rh-Sn/$SiO_2$ samples after simple reduction and after calcination–reduction. The symmetric shape of the imaginary parts and the coincidence between the maxima of the moduli with the maxima of the imaginary parts strongly suggest that, in both samples, the first shell is due to a Sn–*M* contribution only. The spectrum of the sample after calcination and reduction shows a Sn–*M* distance of 2.80 Å, which is 0.05 Å longer than after simple reduction (2.75 Å). As the fit has not been performed on the Sn-edge spectra, the Sn–*M* distances of these samples have been evaluated from the phase-corrected FT spectra.

*Rh–Sn/MgO.* The FT spectrum (not phase corrected) of the Rh–Sn/MgO sample just impregnated exhibits a main peak at 1.57 Å with a weak shoulder at its right side. This peak filtered in the range $\Delta R = 1.21$–$2.30$ Å has been fitted by a two-shell model giving 5 O at 2.055 Å and 1 Cl at 2.31 Å with $\sigma = 0.072$ (the number of independent points is eight, so that for a two-shell fit we can use only seven free parameters; for this reason we have performed the fit by imposing $\sigma_O = \sigma_{Cl}$—the same fit results have been obtained by fixing $N_{tot} = 6$ and keeping the two $\sigma$ independent). The structure around the MgO-supported Rh is completely different from that on silica: almost all the Rh is no longer present in the form of $RhCl_3$ and the metal absorber is surrounded by oxygen atoms at a distance typical of Rh–O bond length in rhodium oxides. It is very well known that a strong interaction may exist between MgO and Cl ions, which are easily stripped from the metal chloride to form surface Mg–Cl sites (27). The FT of the EXAFS signal on the Sn edge indicates that also the Sn is completely present in the form of oxides after the impregnation and no Cl is present around the Sn atoms, either, confirming that all chlorine has migrated to the magnesia surface.

The Fourier-transformed spectrum of the Rh–Sn/MgO sample after calcination (Fig. 6) shows the presence of two shells around the Rh absorber. From the comparison of the FT moduli, both shells seem to overlap with the corresponding ones in the $Rh_2O_3$, but the comparison between the FT imaginary parts of the sample and of the $Rh_2O_3$ clearly shows that: (i) the first peak is due to Rh–O interaction; (ii) the second peak cannot simply be attributed to the Rh–Rh shell of the $Rh_2O_3$. A similar comparison performed with the $RhCl_3$ FT spectrum shows that this peak is not due to the contribution from the Rh–Rh second shell of the

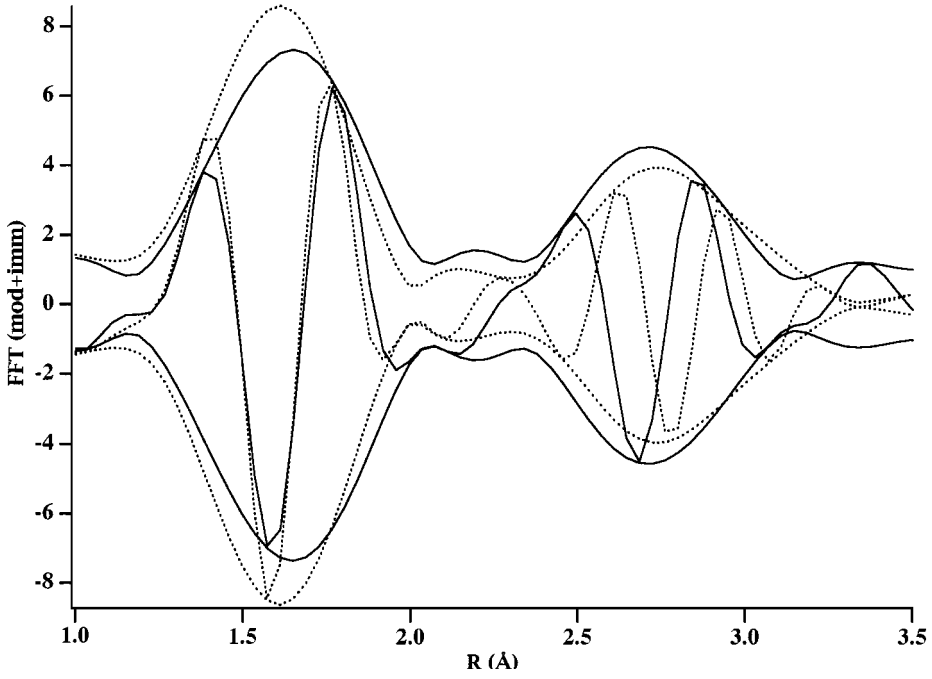


**FIG. 6.** Fourier transform moduli (not phase corrected) of the Rh *K*-edge $k^3$-weighted EXAFS data of Rh–Sn/MgO after calcination (solid line) and of $Rh_2O_3$ (dotted line). $\Delta k = 3.9$–$14$ Å$^{-1}$.

chloride either. This feature can be modelled as a Rh–Mg shell, originated by a migration of a fraction of Rh atoms inside the MgO surface frame, which are then surrounded by Mg atoms as next nearest neighbours (28).

The calcined Rh–Sn/MgO sample after reduction is shown in Fig. 7 compared to those of the Rh foil and $Rh_2O_3$. As well as the Rh–Rh peak corresponding to the first shell of the Rh foil, an additional shell is present at the distance

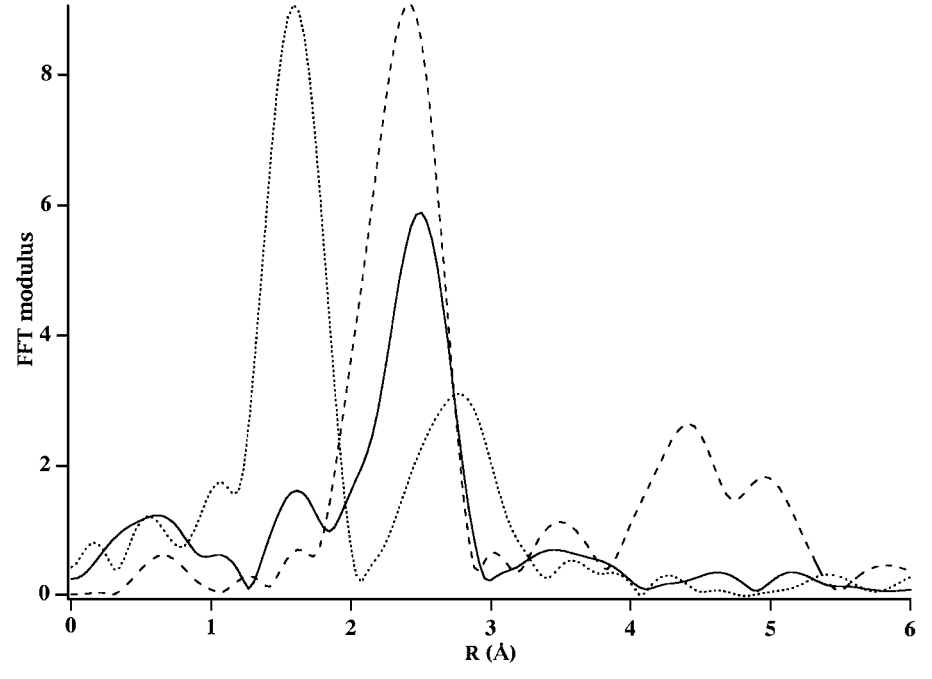


**FIG. 7.** Fourier transform moduli (not phase corrected) of the Rh *K*-edge $k^3$-weighted EXAFS data of Rh–Sn/MgO after reduction (solid line), of Rh foil (dashed line; multiplied by a factor 0.25), and of $Rh_2O_3$ (dotted line). $\Delta k = 3$–$13$ Å$^{-1}$.

of Rh–O in $Rh_2O_3$. The peaks corresponding to the next shells of both Rh foil and $Rh_2O_3$ are absent: the Rh is not present as a bulk oxide, and the metal has no regular fcc structure. The two-shell fit, calculated with experimental phase and amplitude functions, gives 1 O atom at 2.076 Å ($\sigma = 0.094$) and 7.7 Rh atoms at 2.746 Å ($\sigma = 0.114$). The particles are larger than on silica (CN = 7.7 versus 6.8) and with a longer mean Rh–metal distance. The Rh–O residual contribution is thought to be due to the fraction of Rh atoms that are migrated inside the MgO frame and which can no longer be reduced in the standard reductive conditions (28).

The Sn–Sn and Sn–O phase-corrected FT spectrum of the previous sample just after reduction, at the Sn edge, exhibits two distinct peaks, corresponding to a Sn–O shell at 2.16 Å and to a Sn–*M* shell at the same distance as in the silica-supported sample after calcination and reduction (2.80 Å). Also in this case, the distances from the Sn absorber for both shells have been evaluated from the phase-corrected FT spectrum, which also allows estimating that the oxygen shell gives a contribution slightly larger than that of the metal shell in terms of coordination numbers.

### *$H_2$ Chemisorption Measurements*

Table 3 summarises the results of the $H_2$ chemisorption reported in terms of H/Rh ratio, as well as the average coordination numbers of the Rh atoms, as determined by EXAFS. Note that samples at the 2% Rh loading were used for the chemisorption measurements, as this is the highest possible loading for hydrogen chemisorption on MgO without experiencing spillover problems with the pulse chemisorption methodology used in our study. The results show that the distribution of the Rh particles depends on the support used. The H/Rh value for the $SiO_2$-supported sample is higher than on MgO (0.66 vs 0.28). For the bimetallic samples, the H/Rh value is about half the value of the monometallic sample in the case of the Rh–Sn/MgO catalyst, while for the Rh–Sn/$SiO_2$ the value is less than one-tenth. This decrease is less pronounced for the sample after the simple reduction treatment than after the oxidation–reduction cycle at 673 K.

However, the mean particle size is not increased by the presence of tin, as expected from the reduction of the H/Rh value, as the observed coordination number of the Rh–Rh first shell decreases from 10.5 to about 7.

**TABLE 3**

**Hydrogen Chemisorption Data**

| Catalyst[a] | H/Rh | $N^b$ |
|---|---|---|
| Rh/$SiO_2$ | 0.66 | 10.5 |
| Rh–Sn/$SiO_2$ | 0.04 | 6.8 |
| Rh–Sn/$SiO_2$[c] | 0.14 | 7.6 |
| Rh/MgO | 0.28 | — |
| Rh–Sn/MgO | 0.12 | 7.7 |

[a] Rh metal loading = 2 wt%, Sn/Rh molar ratio = 0.5.
[b] Average coordination number measured by EXAFS on samples at 4.0 wt% Rh loading.
[c] Fresh catalyst has been pretreated in $H_2$ flow at 773 K. All the other samples have been exposed to a calcination–reduction cycle at 773 K.

**TABLE 4**

**Catalytic Activity towards Citral Hydrogenation (308 K, 1 atm)**

| Catalyst[a] | Conversion[b] (%) | Selectivity to UOLs (%) |
|---|---|---|
| Rh/$SiO_2$ | 100 | 5.2 |
| Rh–Sn/$SiO_2$ | 57 | 70 |
| Rh–Sn/$SiO_2$[c] | 95 | 11 |
| Rh/MgO | 100 | 0 |
| Rh–Sn/MgO | 45 | 10 |

[a] Rh metal loading = 4 wt%, Sn/Rh molar ratio = 0.5.
[b] Conversion is reported after 24 h from the beginning of the reaction.
[c] Fresh catalyst has been pretreated in $H_2$ flow at 773 K. All the other samples have been exposed to a calcination–reduction cycle at 773 K.

### *Catalytic Activity*

The catalytic properties of the catalysts were evaluated in the selective hydrogenation of $\alpha,\beta$-unsaturated aldehydes. Citral (3,7-dimethyl-2,6-octadienal) was chosen as test molecule. Since a mixture of the isomers E and Z of citral has been used, the corresponding isomeric $\alpha,\beta$-unsaturated alcohols (geraniol and nerol, UOLs) were obtained through the hydrogenation of the carbonyl group. The parallel route via hydrogenation of the conjugated double bond led to the partially saturated aldehyde (citronellal). The only by-product observed was citronellol, according to Scheme 1. The catalytic data are summarised in Table 4.

The monometallic Rh/$SiO_2$ catalyst shows a high activity but a very low selectivity to unsaturated alcohols, with citronellal and citronellol as the main products. The effect of the addition of tin is to significantly decrease the catalytic activity with a corresponding increase in the selectivity to unsaturated alcohols. It is noteworthy that the production of UOLs needs an initial induction period during which the conjugated double bond is predominantly attached. Once UOLs start to be formed, the conjugated C=C hydrogenation rate rapidly decreases with time. The selectivity to UOLs is dependent on the tin content. Preliminary tests had shown that the optimum Sn/Rh molar ratio is 0.5. Additionally, the tin effect was strongly influenced by the activation process on the impregnated catalyst. In fact, after a simple thermal treatment in $H_2$ flow, a Rh–Sn/$SiO_2$ catalyst is obtained whose catalytic behavior is almost the same as that of the monometallic sample. The use of MgO

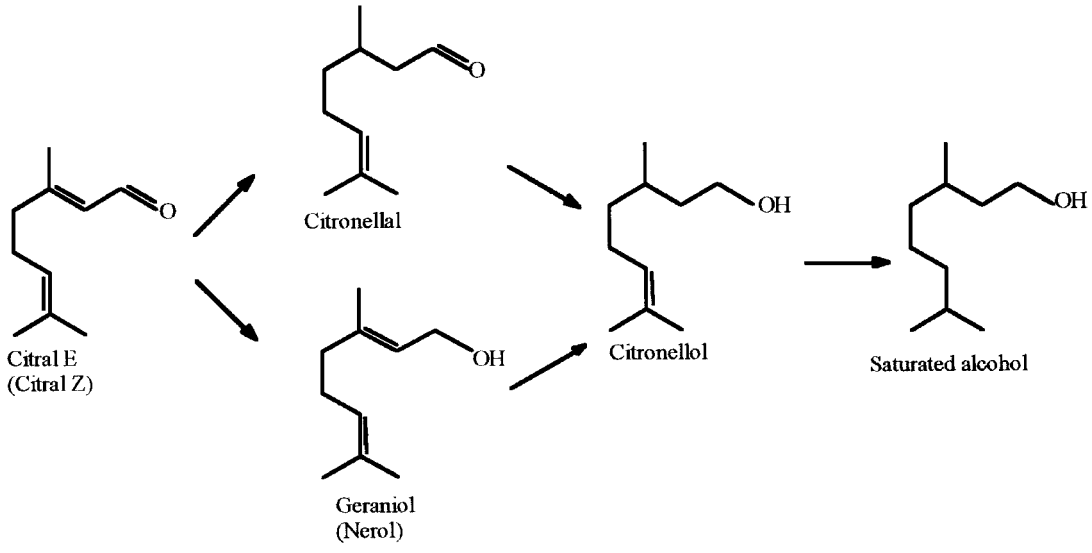


**SCHEME 1**

as support does not increase the selectivity to unsaturated alcohols. The monometallic catalyst shows the same catalytic properties as the silica-supported one. Tin addition to the Rh/MgO catalyst decreases the conversion rate, but this is not compensated by any increase in the selectivity to unsaturated alcohols.

## DISCUSSION

Comparison of the EXAFS data of Rh–Sn/$SiO_2$ and Rh/$SiO_2$ shows that after impregnation the Sn is completely surrounded by oxygen atoms, while the Rh maintains the $RhCl_3$ structure, as it does in the absence of tin.

After calcination, the two samples exhibit different structures at the Rh edge. In particular, two distinct shells for Cl and O are present in the promoted catalyst: the Rh–O distance corresponds to the first shell of the pure $Rh_2O_3$ structure, but the next shell feature suggests the existence of a more complex Rh oxide phase. After reduction, the analysis of the first shell Rh–*M* coordination numbers yields a CN value of 6.8 for the Rh–Sn/$SiO_2$ catalyst, compared to 10.5 for the Rh/$SiO_2$ system. As the Rh and Sn contributions as scattering atoms are not distinguishable, the detected mean CN value represents the overall particle dimension. The higher $\sigma$ factor is attributed to the greater structural static disorder associated with the presence of two atomic indistinguishable species around the absorber atom. These data suggest that the metal particles in Rh–Sn/$SiO_2$ are smaller than those in the Rh/$SiO_2$ catalyst. Interestingly, the chemisorption properties of these bimetallic entities are drastically different from those of the monometallic-supported rhodium. The presence of tin sharply decreases the amount of $H_2$ chemisorbed on rhodium (H/Rh = 0.04 vs 0.66), suggesting a partial coverage (or poisoning) of the exposed rhodium atoms by tin atoms. It seems likely that an incomplete overlayer is formed by the tin atoms, possibly located on the Freundlich sites of the Rh surface (29). As proposed for Pt/$Al_2O_3$ systems (30), a decoration effect can account for the decrease in $H_2$ adsorption capacity much better than the increase of the crystallite diameters.

Since the EXAFS data indicate that the tin ions act as breakers or growth-limiting agents for the metal ensembles (as happens with Cu in Ni or with Ag in Pd catalysts (31, 32)), the sharp decrease in the H/Rh value on the bimetallic particles is not attributable to a particle size effect. The bimetallic particles obtained by simple reduction of the freshly impregnated sample are larger than those formed by calcination and reduction, as shown by the comparison of the first-shell Rh–*M* coordination numbers (7.6 vs 6.8). However, in the former case the rhodium accessibility, as determined by the $H_2$ chemisorption, is much higher (H/Rh = 0.14 vs 0.04).

Thus, we have a situation where the bulk structure, as detected by EXAFS, and the surface structure, detected by the chemisorption measurements, appear to be quite different. The metal dispersion is not simply related to the mean coordination numbers (Table 3). Generally, it is quite difficult to estimate the surface composition of bimetallic catalysts because of the many possible locations of the additive metal on the surface or in bulk of the other metal. The suppressed chemisorption capacity during reduction of Pt/$Al_2O_3$ had been attributed to localised reduction of alumina to form a Pt–Al alloy (33). In the case of Rh and Sn, it is known that Sn can form several substitutional alloys with the fcc structure of Rh metal (34).

The comparison of the first-shell Rh–*M* distance on the two samples suggests that two different bimetallic phases are formed. After calcination and reduction we have a Rh–*M* distance $R = 2.722$ Å, which is 0.035 Å longer than the Rh–Rh foil distance (2.687 Å). After a simple reduction, this distance is $R = 2.752$ Å. As the Sn–Sn first-shell distance in Sn foil is 3.022 Å, we would expect a Rh–Sn distance of 2.854 Å and a decreasing Rh–*M* distance value, down to 2.687 Å, for perfectly segregated Rh and Sn phases. The higher Rh–*M* value observed for the simply reduced sample with respect to the calcined–reduced one suggests a more pronounced alloy character, where each Rh atom is, on the average, surrounded by both Rh and Sn atoms. In the case of the calcined–reduced sample, the lower Rh–*M* distance value indicates a situation closer to a cherry-like structure, where each Rh atom is predominantly surrounded by other Rh atoms and the Sn atoms are mostly located at the external metallic surface. The Sn–*M* distance, evaluated from the phase-corrected FT spectra on the Sn edge, supports this interpretation. The Sn–*M* distance is in fact greater in the calcined–reduced sample than in the simply reduced one, confirming that in the former sample the Sn is on the average surrounded by a greater number of Sn atoms which are not intercalated with Rh atoms. From the comparison of the EXAFS data and the chemisorption properties of the two silica-supported bimetallic systems, it can be concluded that on the simply reduced sample a tin-enriched phase is preferentially located at the more external particle lattice layers. Instead, on the calcined–reduced sample there are some "patches" of Sn aggregates decorating the Rh particle surface. The difference in the chemisorption properties is then due to a different surface composition, which, in turn, is a consequence of the different degree of Rh–Sn interaction in the bimetallic entities formed during the activation treatments.

The structural differences in surface tin distribution obviously influence also the catalytic behavior: the sample after the calcination–reduction activation shows a much higher selectivity to UOLs (Table 4). This high selectivity to C=O bond hydrogenation is, however, reached after an induction period, during which conventional C=C hydrogenation is observed. This behavior has already been observed in the selective hydrogenation of $\alpha,\beta$-unsaturated aldehydes with various catalytic systems, including Ru–Sn/$Al_2O_3$ (12) and Pt–Sn catalysts (35). In the latter case, it was suggested that during this induction period a surface restructuring occurs, where the $Sn^0$ is partially converted to $Sn^{n+}$ by the reaction mixture.

In our case, a similar explanation can be advanced in the citral hydrogenation. The positive effect of tin is mainly related to the formation, during the coadsorption of reactants and products, of tin oxides decorating part of the rhodium surface. It is interesting to observe that the catalyst surface restructuring depends on the starting surface structure. The process preferentially occurs with a cherry-like structure, whereas in the alloy-type phase the decreased affinity to oxygen of the tin atoms largely prevents this localised oxidation.

Our results thus suggest that an alloy structure cannot work in the selective hydrogenation reactions due to the lack of $Sn^{\delta+}$ sites. Remarkably, Didillon *et al.* (36) reported that their active and selective Rh–Sn/$SiO_2$ catalysts after a treatment under $H_2$ at 773 K were totally unselective, and their XPS studies revealed the presence of zerovalent Rh–Sn in the particles (37). Also, Ponec pointed out that it seems a priori impossible that the use of alloys as catalysts should improve the selectivity to UOLs (7).

The induction period could then be related to two mechanisms: (i) the chemisorption and the further reactivity between the zero valent Rh–Sn particles and the aldehyde CO group, as proposed by Iwasawa and Yoshikawa on the basis of an in situ Sn *K*-edge EXAFS study upon acetophenone adsorption (14); (ii) the tin oxidation by silica surface silanols and by water traces, as proposed by Candy *et al.* (36a). In our case the mechanism (ii) is probably favored by the presence of moisture traces during the reactor loading procedures.

The catalytic data obtained with the alloy-type phase also indicate that there are no other relevant electronic effects, such as an increase in the electron density on the rhodium atoms due to the formation of the Rh–Sn alloys. With respect to these possible electronic effects, the use of a basic support, such as MgO, should lead to the formation of electron-rich metal particles (38), resulting in an enhanced UOLs selectivity. This interpretation was proposed to explain why the graphite-supported platinum has a much better selectivity in cinnamaldehyde hydrogenation than the charcoal-supported platinum (4). However, in our situation it appears quite clear that no relevant support effect occurred, since the two unpromoted Rh/$SiO_2$ and Rh/MgO catalysts behave in almost the same way. The decreased extent of exposed rhodium atoms in Rh/MgO, as measured by $H_2$ chemisorption, can be due either to the contamination of the metal surface by chlorine or to the decrease of the Rh atoms accessibility. The contamination by Cl is a well-known phenomenon (39), since noble metal catalysts are typically prepared using a chlorine-containing catalyst precursor salts. However, the EXAFS data just after the impregnation indicate that almost all the chlorine atoms have migrated onto the magnesia surface to form Mg–Cl sites, so that only a small fraction of the Cl can contribute to the $H_2$ chemisorption decrease. On the other hand, after calcination, a fraction of the Rh atoms are known to migrate inside the support surface (28) and, as they cannot be reduced any more in $H_2$ at 773 K, their contribution to the $H_2$ chemisorption is absent. This factor can account for

the reduced chemisorption capacity when MgO is used as support.

The first-shell Rh–*M* distance of 2.746 Å, detected by EXAFS for the Rh–Sn/MgO sample after reduction (vs the 2.722 Å of the cherry-type Rh–Sn/$SiO_2$), indicates the formation of an alloy-type structure also for the MgO-supported catalyst. In the case of magnesia, this hypothesis is confirmed by the observation that after the addition of tin the H/Rh value is half that in the absence of tin. The presence of an alloy-type structure reflects also the high value of $\sigma$ on MgO, which suggests that the distance we measure is actually an average between two different unresolved distances.

The close similarity of the Rh–*M* distances between the Rh–Sn/$SiO_2$ catalyst after simple reduction and the Rh–Sn/MgO sample, where the presence of an alloy-type phase is confirmed also by the chemisorption data, strengthens the proposed alloy-type model for the silica-supported catalyst. In agreement with the behavior on silica, in the case of the magnesia the alloy particles are almost totally unselective towards UOLs.

## CONCLUSIONS

The bimetallic Rh–Sn/$SiO_2$ catalysts were characterised by in situ EXAFS investigation. Different morphological structures evolved as a function of the activation treatments applied to the freshly prepared catalysts. Two models, depending on the extent of Rh–Sn interactions, may explain the selectivity differences in the selective hydrogenation of citral:

- a cherry-like structure, obtained by calcination–reduction treatments, where part of the tin aggregates in patches decorating the rhodium particle surface; in this case, the catalyst properties seem to be due to a surface restructuring, induced by the coadsorption of reactants, products, and moisture, where $SnO_x$ moieties are produced on the rhodium surface;
- an alloy-type phase, obtained by a simple reduction treatment, in which a tin-enriched phase is preferentially located at the more external particle lattice layers; the formation of such an alloy-type phase hinders the formation of active $SnO_x$ sites, leading to an unselective catalyst.

At the end of the induction period, the enhanced UOLs selectivity, following the activation by calcination–reduction treatment, is attributed to the electron pair donor–acceptor interaction of the carbonyl group with the Lewis acid sites present in tin oxides decorating the rhodium particle surface.

## ACKNOWLEDGMENTS

This work was partially supported by the CNR. The authors thank the ESRF of Grenoble for the provision of synchrotron radiation under the EEC Grant CH-163 and the staff of the GILDA beamline for technical assistance.

## REFERENCES

1. Rylander, P. N., "Catalytic Hydrogenation over Platinum Metals." Academic Press, New York, 1967.
2. Giroir-Fendler, A., Richard, D., and Gallezot, P., *in* "Heterogeneous Catalysis and Fine Chemicals" (M. Guisnet *et al*., Eds.), p. 171. Elsevier, Amsterdam, 1988.
3. Richard, D., Ockelford, J., Giroir-Fendler, A., and Gallezot, P., *Catal. Lett.* **3**, 53 (1989).
4. Giroir-Fendler, A., Richard, D., and Gallezot, P., *Catal. Lett.* **5**, 175 (1990).
5. Mercadante, L., Neri, G., Milone, C., Donato, A., and Galvagno, S., *J. Mol. Catal.* **105**, 93 (1996).
6. English, M., Jentys, A., and Lercher, J. A., *J. Catal.* **166**, 25 (1997).
7. Ponec, V., *Appl. Catal.* **49**, 27 (1997).
8. (a) Ponec, V., and Bond, G. C., "Catalysis by Metals and Alloys," Studies in Surface Science Catalysis, Vol. 95. Elsevier, Amsterdam, 1995; (b) Sachtler, W. M. H., *J. Mol. Catal.* **25**, 1 (1984); (c) Paál, Z., Györy, A., Uszkurat, I., Olivier, S., Guérin, M., and Kappenstein, C., *J. Catal.* **168**, 164 (1997).
9. Correa, F., Nakamura, R., Stimson, R. E., Burwell, R. L., Jr., and Shriver, D. F., *J. Am. Chem. Soc.* **102**, 5112 (1980).
10. Augustine, R. L., and Meng, L., *in* "Catalysis of Organic Reactions" (R. E. Malz, Jr., Ed.), p. 15. Dekker, NewYork, 1996.
11. Didillon, B., Candy, J. P., El-Mansour, A., Houtman, C., and Basset, J. M., *J. Mol. Catal.* **74**, 43 (1992).
12. Neri, G., Mercadante, L., Milone, C., Pietropaolo, R., and Galvagno, S., *J. Mol. Catal.* **108**, 41 (1996).
13. Tomishige, K., Asakura, K., and Iwasawa, Y., *J. Catal.* **149**, 70 (1994).
14. Iwasawa, Y., and Yoshikawa, K., *J. Mol. Catal.* **100**, 115 (1995).
15. Sinfelt, J. H., Via, G. H., and Lytle, F. W., *J. Chem. Phys.* **68**, 2009 (1978); Via, G. H., Sinfelt, J. H., and Lytle, F. W., *J. Chem. Phys.* **71**, 690 (1978); Van't Blik, H. F., Van Zon, J. B. A. D., Huizinga, T., Vis, J. C., Koningsgerger, D. C., and Prins, R., *J. Phys. Chem.* **87**, 2264 (1983).
16. Meitzner, G., Via, G. H., Lytle, F. W., Fung, S. C., and Sinfelt, J. H., *J. Phys. Chem.* **92**, 2925 (1988); Van Gruijthuijsen, L. M. P., Howsman, G. J., Delgass, W. N., Koningsberger, D. C., Van Santen, R. A., and Niemantsverdriet, J. W., *J. Catal.* **170**, 331 (1997).
17. Bellatreccia, M., Zanoni, R., Dossi, C., Psaro, R., Recchia, S., and Vlaic, G., *J. Chem. Soc. Faraday Trans.* **91**, 2045 (1995); Thomas, J. M., *Chem. Eur. J.* **3**, 1557 (1997).
18. Sermon, P. A., *J. Catal.* **24**, 467 (1972).
19. Dossi, C., Fusi, A., and Russo, O., *Analysis Europa*, 17 (Apr. 1995).
20. Pascarelli, S., Boscherini, F., D'Acapito, F., Hardy, J., Meneghini, C., and Mobilio, S., *J. Synchrotron Rad.* **3**, 147 (1996).
21. S. S. Hasnain (Ed.), "X-Ray Absorption Fine Structure," p. 751. Ellis Horwood, Chicester, 1991.
22. Lengeler, B., and Eisenberger, E. P., *Phys. Rev. B* **21**, 4507 (1980).
23. Michalowicz, A., *J. Phys. IV Fr.* 7C2-235, 1997.
24. James, F., and Roos, M., *Comput. Phys. Commun.* **10**, 343 (1975).
25. Joyner, R. W., Martin, K. H., and Meehan, P., *J. Phys. C* **20**, 4005 (1987).
26. Gloor, A. P., and Prins, R., *J. Phys. Chem.* **98**, 9865 (1994).
27. Kappers, M., Dossi, C., Psaro, R., Recchia, S., and Fusi, A., *Catal. Lett.* **39**, 183 (1996).
28. Cepparo, A., Thesis, University of Trieste, Italy, 1997.
29. Sachtler, W. M. H., and Ichikawa, M., *J. Phys. Chem.* **90**, 4752 (1986).

30. Dautzenberg, F., and Wolters, H. B. M., *J. Catal.* **51**, 26 (1978).
31. Soma-Noto, Y., and Sachtler, W. M. H., *J. Catal.* **32**, 312 (1974).
32. Primet, M., Mathieu, M. V., and Sachtler, W. M. H., *J. Catal.* **44**, 324 (1976).
33. Ren-Yuan, T., Rong-An, W., and Li-Wu, L., *Appl. Catal.* **10**, 163 (1984).
34. Chojnacki, T. P., and Schmidt, L. D., *J. Catal.* **129**, 473 (1991).
35. Marinelli, T. B. L. W., and Ponec, V., *J. Catal.* **156**, 51 (1995).
36. Didillon, B., El-Mansour, A., Candy, J. P., Bournoville, J. P., and Basset, J. M., *in* "Heterogeneous Catalysis and Fine Chemicals II" (M. Guisnet *et al.*, Eds.), p. 437. Elsevier, Amsterdam, 1991.
37. (a) Candy, J. P., Ferretti, O. A., Mabilon, G., Bournoville, J. P., El-Mansour, A., Basset, J. M., and Martino, G., *J. Catal.* **112**, 210 (1988); (b) Didillon, B., Houtman, C., Shay, T., Candy, J. P., and Basset, J. M., *J. Am. Chem. Soc.* **115**, 9380 (1993).
38. Dossi, C., Psaro, R., Bartsch, A., Fusi, A., Sordelli, L., Ugo, R., Bellatreccia, M., Zanoni, R., and Vlaic, G., *J. Catal.* **145**, 377 (1994).
39. Bartholomew, C. H., *in* "Catalysis" (J. J. Spivey and S. K. Agarwal, Eds.), Vol. 11, p. 111. The Royal Society of Chemistry, Cambridge, UK, 1994.